

**EXPERIMENTAL STUDY OF THERMAL LOADING ON A PLATE FROM A TRIPLE
ROUND JET ARRAY**

by

Pau Jeffrey Kristo

Bachelor of Science, University of Pittsburgh, 2013

Submitted to the Graduate Faculty of
Swanson School of Engineering in partial fulfillment
of the requirements for the degree of
Master of Science

University of Pittsburgh

2015

UNIVERSITY OF PITTSBURGH
SWANSON SCHOOL OF ENGINEERING

This thesis was presented

by

Paul Jeffrey Kristo

It was defended on

November 18, 2015

and approved by

John Brigham, Ph.D., Associate Professor, Department of Civil & Environmental
Engineering, University of Pittsburgh

David Schmidt, Ph.D., Assistant Professor, Department of Mechanical Engineering &
Materials Science, University of Pittsburgh

Thesis Advisor: Mark Kimber, Ph.D., Associate Professor, Department of Mechanical
Engineering & Materials Science, University of Pittsburgh

Copyright © by Paul Kristo

2015

**EXPERIMENTAL STUDY OF THERMAL LOADING ON A PLATE FROM A
PARALLEL ROUND JET ARRAY**

Paul Kristo, M.S.

University of Pittsburgh, 2015

Temperature fluctuations are known to occur in the mixing region of non-isothermal flows, and can cause undesired thermal stresses. One relevant application where this is a major concern is the very high temperature gas reactor (VHTR), a next generation nuclear reactor, which uses helium as the primary coolant. In the lower plenum of the VHTR, coolant enters from multiple channels at different temperatures and mixes together before being routed to a gas turbine or hydrogen production facility. Incomplete mixing of the coolant can be the root of thermal stresses both within the lower plenum as well as downstream components (e.g., gas turbine blades). For acceptable predictions of this phenomenon, fundamentally based experiments along with properly verified and validated models are needed. The objectives of this study are to gain insight into the thermal loading conditions expected in the VHTR lower plenum and provide valuable experimental validation data for current and future modeling efforts. To this end, an experimental study is conducted for three non-isothermal parallel round jets whose axis to axis separation distance is 1.41 jet diameters. A central cold jet is surrounded on either side by an adjacent hot jet in a planar configuration with air as the working fluid. All of the jets are turbulent with a jet Reynolds number between 5.5×10^3 and 1.8×10^4 , and the mixing is quantified via temperature measurements on a flat polycarbonate plate mounted parallel to the axial direction of the jets. The full field temperatures of the plate surface are captured via infrared thermography. Two different plate to

jet spacings are considered: 0.5 and 1.0 jet diameters. Other variables include the cold to hot jet velocity ratio, set at three levels of 0.50, 1.00, and 1.51, and the temperature difference between the cold and hot jets, set at two different values of 33.3°C and 44.4°C. Horizontal line traces of the plate surface temperature are analyzed in the range of 2-20 jet diameters downstream. The line traces suggest that with decreasing velocity ratios, the induced turbulence provided by higher jet velocities promotes mixing further upstream. Results also suggest the most severe temperature gradients on the plate surface occur in the area that is characteristic of the convective mixing region (8 to 16 jet diameters downstream). Observations of the maximum surface temperature on the plate describe the influence of the plate to jet spacings in the entrance region (2 to 8 jet diameters downstream) in that with increased spacing, the maximum temperatures are closer to the axial center of the cold jet. Past the entrance region and with increasing values of jet velocity ratio, the maximum temperature location spreads much more rapidly. The thermal mixing initiated further upstream by increasing values of jet velocity ratios and the rapid spreading of maximum plate surface temperatures for decreasing jet velocity ratios are both notable concerns in the analysis of reactor coolant channel outlet conditions and their thermal hydraulic interactions with solid boundaries. This research represents preliminary predictions of the thermal loading in the VHTR lower plenum and provides validation data for fundamental and applied thermal mixing simulations.

TABLE OF CONTENTS

PREFACE.....	XI
NOMENCLATURE.....	XII
SUBSCRIPTS	XIII
1.0 INTRODUCTION.....	1
2.0 EXPERIMENT.....	6
2.1 EXPERIMENTAL FACILITY	6
2.2 EXPERIMENTAL PARAMETERS.....	10
2.3 EXPERIMENTAL METHODS	15
3.0 RESULTS	17
3.1 TEMPERATURE PROFILE CASE STUDY	17
3.2 TEMPERATURE LINE TRACE COMPARISON.....	22
3.3 LOCATIONS OF MAXIMUM TEMPERATURE	37
4.0 CONCLUSIONS	41
BIBLIOGRAPHY	44

LIST OF TABLES

Table 1: Experimental conditions	13
Table 2: Maximum average asymmetric error across all line traces for each case.....	24
Table 3: Total uncertainty in non-dimensionalized temperature for case 4.....	27

LIST OF FIGURES

Figure 1: Turbulent triple jet configuration with thermal mixing regions and notable hydraulic characteristics of a singular jet (original Figure 9-3 from [7] has been edited to include approximate thermal mixing regions).....	3
Figure 2: Isometric view of test section including (1) parallel triple jets (2) jet spacing plate (3) angled mount (4) plug (5) viewports (6) parallel wall.....	6
Figure 3: Process flow diagram of external temperature and flow control skid.....	8
Figure 4: Transparent jets with honeycomb flow straighteners and cross section displayed	10
Figure 5: Top view of triple jet test section and confining wall with highlighted spacing parameters	12
Figure 6: Front view of test section and IR viewports with non-dimensional axial directions highlighted	14

Figure 7: Contours of triple jet-induced temperature fields across parallel wall for $\Delta T = 44.4^\circ\text{C}$ and $\delta = 0.5$. Approximate size of each image is 13.4 cm x 17.1 cm (a) $R = 0.5$ port 1 (b) $R = 1.0$ port 1 (c) $R = 1.5$ port 1 (d) $R = 0.5$ port 2 (e) $R = 1.0$ port 2 (f) $R = 1.5$ port 2 (g) $R = 0.5$ port 3 (h) $R = 1.0$ port 3 (i) $R = 1.5$ port 3.....	18
Figure 8: Time-averaged temperature contours and corresponding temperature fluctuations from Kimura et al. [11].....	21
Figure 9: (a) Case 4, port 1 temperature field with imposed line traces (b) Case 4, port 1 polycarbonate plate line trace surface temperatures	23
Figure 10: Total uncertainty range for $X^*=2$ line trace of case 4	28
Figure 11: Line temperature profiles with fixed $\Delta T = 44.4^\circ\text{C}$ and $\delta = 0.5$	30
Figure 12: Temperature difference and plate spacing comparison in three characteristic flow regions.....	34
Figure 13: Case 10, port 1 temperature field with imposed line traces	35

Figure 14: Peak temperature location for each line temperature trace with imposed hot jet center
line..... 38

PREFACE

This research is being performed using funding received from the DOE Office of Nuclear Energy's Nuclear Energy University Programs.

NOMENCLATURE

X	axial direction
ν	degrees of freedom of fit
D	diameter (of jet unless otherwise noted)
ϵ	emissivity
ε	error
L	length
X^*	non-dimensional axial direction
Y^*	non-dimensional radial direction
θ	non-dimensional temperature
N	number of sets of measurements
δ	plate spacing
S	scaled jet spacing
s	standard deviation
t	student's t-distribution
Y	radial direction
Re	Reynolds number
T	temperature
ΔT	temperature difference between cold and hot jet outlets

U uncertainty
V velocity
R velocity ratio

SUBSCRIPTS

asym asymmetric
cal calibration
C cold jet
cell hexagonal honeycomb cell
H hot jet
hc honeycomb
hyd hydraulic
LHS left-hand side
m mean
o outlet
prec precision
rep repeatability
res resolution

RHS right-hand side

tot total

1.0 INTRODUCTION

The turbulent mixing of hot and cold fluids experience thermal fluctuations within the mixing region. These temperature fluctuations are transmitted to the supporting structure and can cause severe high cycle thermal fatigue over the course of a component's operational lifetime, a process also known as thermal striping. In both existing and next generation nuclear reactor designs, this has been and continues to be a major focus of study. Over the course of a reactor's lifespan, the effects of thermal striping can jeopardize the structural integrity of the nuclear reactor core. Thermal striping is a particular concern in the Generation IV very high temperature gas reactor (VHTR), which employs helium as a coolant. Using a gas for the coolant enables natural convective cooling under accident scenarios, but can alternatively produce higher thermal fluctuations than modern pressurized water reactors (PWRs). The helium extracts heat throughout the core before mixing in the lower plenum in a confined series of jets. These jets enter the lower plenum at different temperatures (on the order of 300°C [1, 2]) caused by the non-uniform heat generation in the reactor core. In addition, the inability to evenly distribute the flow through the hundreds of coolant channels produces a range of jet velocities, which further complicates the mixing.

The issue of thermal striping in nuclear reactors was first identified as a major cause of structural fatigue in the early 1980s [3-5]. Lloyd and Wood [5] first presented the issue in their analysis on the initiation and subsequent propagation of surface cracks in a stainless steel section

subjected to high frequency thermal shocks. Thermal shocking is defined as the condition in which the surface temperature change has occurred before the effects have significantly penetrated into the component wall [4]. With repeated thermal shocks, the thermal striping experienced by internal wall components becomes more severe over time. A standard approach to quantify the underlying flow physics and loading during thermal striping is to study arrays of parallel jets, which also serves as the basis for this investigation.

A common configuration seen in previous experimental and numerical investigations is that of a parallel triple jet. This has been studied for “quasi-free jets” (i.e., where solid walls or boundaries are far removed from the jets), as well as for thermal and fluid interactions with solid components in close proximity. Tokuhiro and Kimura [6] conducted experiments using a triple slot jet configuration including a central cold jet (non-buoyant) and a hot jet on either side (considered buoyant) with water as the working fluid. They compared the behavior to that of reference single jet. Three regions of flow were studied: (1) the “entrance” region where temperature was considered constant (negligible increase in cold jet temperature or decrease in hot jet temperature), (2) the “convective mixing” area where the temperature increase/decrease has become significant, and (3) the “post mixing” region where the temperature assumes an asymptotically decreasing trend [6]. A visual representation of the general triple jet configuration and these corresponding thermal regions is provided in Figure 1, which was edited from the original figure of a submerged turbulent jet from [7]. For reference, the notable features of an individual jet and expected velocity profiles (at approximate downstream lengths) are also included, however it should be noted that sufficiently far downstream, the three jets form a singular composite jet.

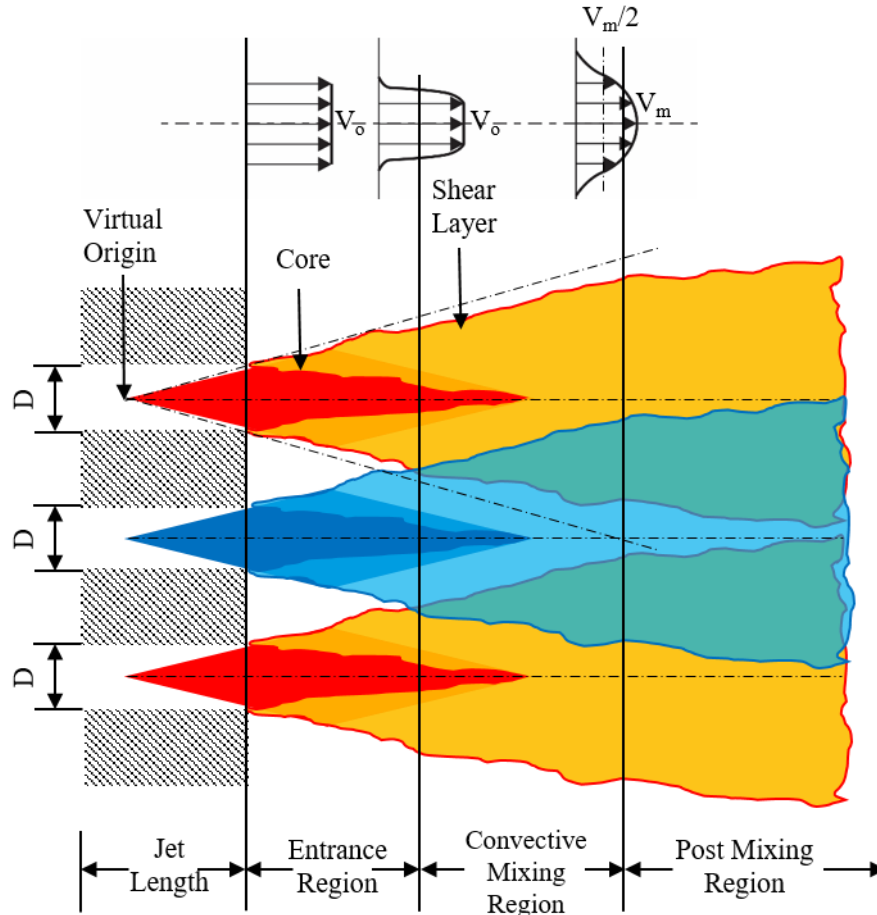


Figure 1: Turbulent triple jet configuration with thermal mixing regions and notable hydraulic characteristics of a singular jet (original Figure 9-3 from [7] has been edited to include approximate thermal mixing regions)

Several numerical studies were produced based on this preliminary experimental work [8-10]. Kimura et al. [10] compared the low Reynolds number turbulent stress and heat flux equation models (LRSFM), standard two-equation $k-\epsilon$, and quasi-direct numerical simulation (DNS) turbulence models to an isovelocity water experiment using a triple slot jet configuration similar to that of [6]. In comparison to the experimental data, the DNS and LRSFM models provided the closest simulation to the expected flow physics, with the DNS providing the best comparison of the temperature fluctuation intensity and time trends of temperature. More recently, Cao et al [8],

provided a numerical comparison to the experimental model presented in [6] using ANSYS Fluent software with large eddy simulation (LES). The numerical simulation provided an agreeable solution to the experimental data with an improved understanding of the turbulent behavior's influence on the temperature fluctuations in the fluid. It was concluded that vortices are closely related to the temperature fluctuation phenomenon as expected, and that by increasing the Reynold's number, the mixing of hot and cold flows is delayed while the convective mixing region is enlarged.

Several experimentally-validated numerical studies have also been performed to analyze the interaction of multiple parallel jets with basic geometric components [11-15]. One of the most notable of these studies is that performed by Kimura et al. [11] in which parallel slot jets were sandwiched between two stainless steel walls. The working fluid in this case was sodium. By assuming a constant heat transfer coefficient in the plate, thermal striping could be characterized by a transfer function of temperature fluctuation between two positions in the wall. The temperature fluctuation at a given wall location was based on the Fourier transform of measured temperature history in that wall position. The transfer function was derived from the non-stationary one-dimensional thermal conduction equation. This approach allowed each frequency to be expressed independent of other frequency components, and allowed the temperature signal at a given point in the wall to be quantified as the linear combination of all frequency components. It was concluded that the theoretical solution was in good agreement with the experimental results. Interestingly, the contours of time-averaged temperature and fluctuation intensity in the higher discharged velocity case were found to be similar to those in the lower velocity case.

The primary focus of these studies has been the flow physics and thermal fluctuations present in slot jets, due to their applicability in liquid metal fast reactors [5, 6, 8-13, 16]. Although

qualitatively similar, round jets exhibit fundamentally different flow physics (e.g., jet decay and spreading rate as shown in [17], [18]) and are not just of interest in the prismatic VHTR lower plenum, but are encountered in other applications, including flame base topology in combustion applications [19], the influence of acoustic excitation on the heat transfer and flow behavior of a round impinging jet [20], and electronic cooling with the use of synthetic round jet impingement [21]. While these experimental studies provide a better understanding of the underlying flow physics of a singular round jet in various applications, the lack of experimental and numerical work done with multiple turbulent round jets leaves more analysis to be desired. This is of particular concern regarding the jet outlets found in the lower plenum of the prismatic VHTR.

For primary validation efforts with respect to thermal loading in the plate, the time averaged thermal signatures are required. The subject of multiple turbulent circular jets is of great significance in the study of the VHTR lower plenum for several different cases. Several experimental studies have been conducted regarding flow visualization of VHTR components subject to jet impingement including [22-24]. Likewise, experimental-validation for computational modeling of accident scenarios of the VHTR have been examined [25, 26]. Although these and other studies provide insight into unique flow conditions and characteristics, a slightly different approach is also worthwhile. For validation purposes, the planned experiments should focus on relevant, yet simplistic configurations, rather than try to include all the complexities of the actual application. Without a fundamentals-based experiment, it becomes difficult to validate computational models and their underlying assumptions since the geometric requirements of the mesh could drastically increase the computational cost beyond desired levels. Therefore, the secondary contribution of the current work is to provide such data for a triple parallel round jet near a solid wall.

2.0 EXPERIMENT

2.1 EXPERIMENTAL FACILITY

The in-house experimental facility allows for a series of three round jets to flow parallel to an adjacent wall. Figure 2 provides a visual representation of the experimental setup.

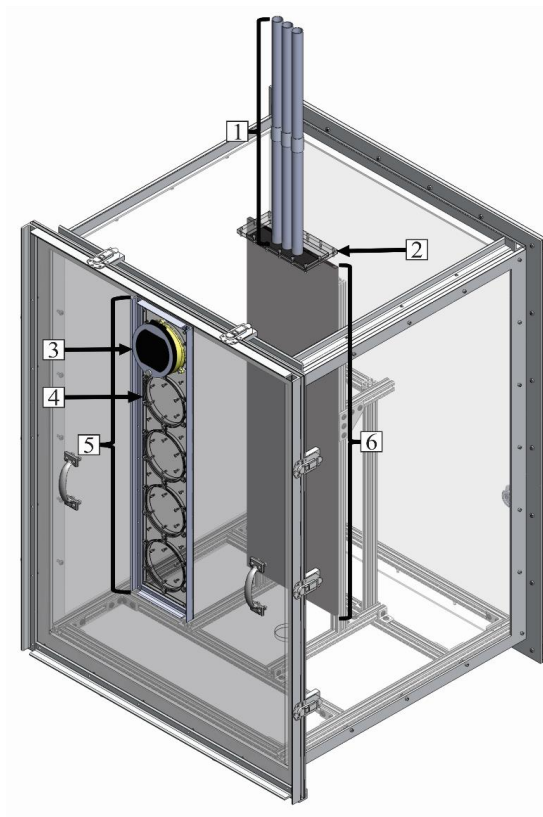


Figure 2: Isometric view of test section including (1) parallel triple jets (2) jet spacing plate (3) angled mount (4) plug (5) viewports (6) parallel wall

The facility includes a 73.7 cm x 76.2 cm x 106.7 cm enclosed test section with (as referenced in Figure 2) three parallel round jets whose outlets are located on the top surface of the test section which are fixed to the appropriate jet spacing at the inlet of the test section via a jet spacing plate. The front surface of the test section incorporates an angled mount, which holds a broadband crystal lens, and four polycarbonate plugs all housed in five separate viewport locations. Inside the test section is the parallel wall of dimensions 27.9 cm x 96.5 cm x 0.9 cm which is fixed via a structural support frame. The parallel wall is composed of polycarbonate and is painted with Krylon 1602 paint having an emissivity (ϵ) of 0.95 [27]. The polycarbonate plate has a melting temperature of 155°C and a thermal conductivity of 0.19 W m⁻¹ K⁻¹, which minimizes the thermal smearing (lateral conduction) and enables a clear thermal signature to be revealed on the surface. The use of these experimental components is expanded in the proceeding sections in regards to measuring the surface temperature on the parallel wall. The three parallel jets are fixed vertically via a structural support frame and are connected to a corresponding external temperature and flow control skid. A process flow diagram of the external temperature and flow control skid is included in Figure 3.

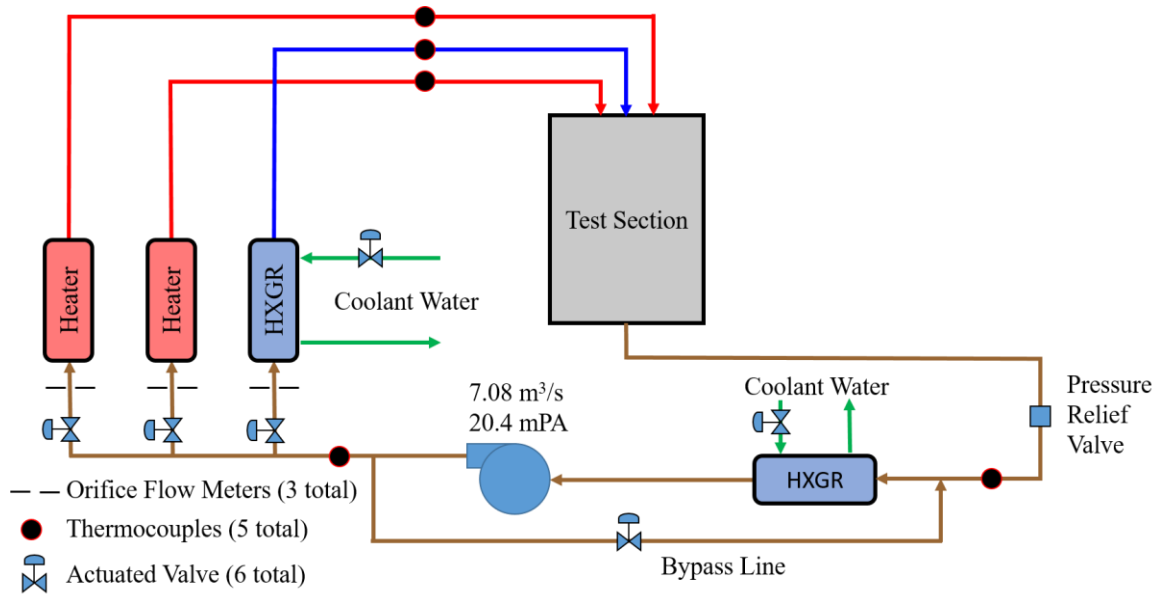


Figure 3: Process flow diagram of external temperature and flow control skid

The temperature and flow control skid includes two separate heaters for the two outermost jet lines and a heat exchanger (cooled with a secondary water line) for the center jet line with flow for all three lines produced by a blower. The blower is capable of motivating $7.08 \text{ m}^3/\text{s}$ at an operating pressure of $2.04 \times 10^4 \text{ Pa}$. The test section's outer support frame includes rubber feet to dampen any type of unwanted vibrational response from the surrounding environment. At the bottom of the test section, a 5.08 cm line allows air to exit the facility. The exit line at the bottom of the test section returns to the temperature and flow control skid, forming a closed loop. An additional system heat exchanger is included to regulate unwanted increases in jet temperatures from downstream mixing and re-entry of the flow in the blower.

The flow control skid utilizes air as the working fluid. The volumetric flow of the individual jets are held constant by the temperature and flow control skid's automated valves after the jet temperatures reach steady state, which for the current study, provides a worst case uncertainty of $\pm 1.6\%$. The jet outlet conditions are also of considerable interest, for both the current

investigation and future use in numerical modeling validation. Landfried [28] performed a study in which the velocity profiles, turbulence statistics, and temperature profiles at the outlet of an individual jet were quantified using hot wire anemometry in conjunction with an additional cold wire for temperature compensation. The study was performed using comparable flow rates and temperatures as found in the present work. It was found that an individual jet outlet consists of a velocity profile akin to a power law fit and that the jet outlet turbulence parameters are analogous to the velocities found there. It was determined that the average turbulence intensity across the diameter of the jet outlet is 8.55%. Additionally, temperature traces across the outlet of the jet provide that the mean temperature across the measurement intervals varies by 2.6% across 90% of the full jet diameter, concluding that the jet outlet consists of a tophat temperature profile. Additional details regarding the temperature and flow control setup as well as a more detailed review of the jet outlet velocity, turbulence, and thermal characteristics can be found in [28]. The jets themselves consist of two 30.48 cm long pipes with internal diameters of 2.22 cm connected via a custom coupling. Inside each coupling is a honeycomb insert for flow straightening and improved uniform turbulence quantities as seen in Figure 4.

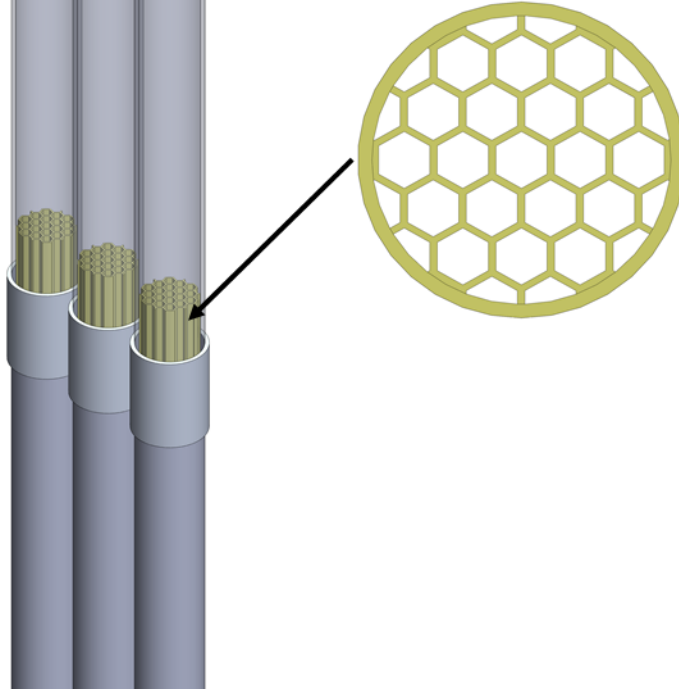


Figure 4: Transparent jets with honeycomb flow straighteners and cross section displayed

The honeycomb flow straighteners are composed of Somos[®] NanoTool. The honeycomb flow straightener length is $L_{HC} = 76.20$ mm and the hydraulic diameter of an individual hexagonal cell is $D_{hyd,cell} = 3.74$ mm, such that $L_{HC}/D_{hyd,cell} = 20.4$. The area of each honeycomb hex cell is 12.11 mm², the ligament thickness is 0.56 mm, and there are a total of 19 full cells in the center and 12 partial cells around the perimeter of an individual flow straightener as seen in Figure 4.

2.2 EXPERIMENTAL PARAMETERS

The three jets consist of a center cold jet with an adjacent hot jet on either side. The hot jets are each consistently set to the same temperatures and flow rates for their respective test case. The test cases are categorized by the velocity ratio (R) between the cold and hot jets, defined as

$$R = \frac{V_C}{V_H} \quad (1)$$

Where V_C is the velocity of the cold jet and V_H is the velocity of each hot jet. Each velocity ratio R is subject to a temperature difference between the jets, defined as

$$\Delta T = T_H - T_C \quad (2)$$

Where T_H is the outlet temperature of the hot jets and T_C is the outlet temperature of the center cold jet. For this experimental study, the two prescribed temperature differences between the jets are $\Delta T = 33.3^\circ\text{C}$ and $\Delta T = 44.4^\circ\text{C}$. Additionally, two physical spacings are defined. The plate spacing, δ is the separation distance between the plate surface and the axial centerline of the three jets. For this experimental study, two spacings are considered: one where the plate surface is fixed directly tangent to the outlet of the jets ($\delta = 0.5$) and one jet diameter away ($\delta = 1.0$). The jet spacing, S , is the relative inline distance of the jet centers from one another and is based on a scaled mock-up of the General Atomics gas turbine modular helium reactor (GT-MHR) [29]. The scaled jet spacing for this study is fixed $S = 3.13$ cm. It should be noted that the General Atomics GT-MHR consists of a prismatic core design in which the outlets of the jets in the lower plenum are in hexagonal configurations. While the prismatic core design consists of staggered arrays of jets in relative 120° triangles, the more fundamental 180° (planar) triple jet configuration used here provides a better preliminary analysis to compare against previous non-isothermal triple jet data as discussed prior, and to offer experimental conditions more easily used for computational validation efforts. A visual representation of the plate spacing ($\delta = 0.5$) and jet spacing ($S = 3.13$ cm) can be seen in Figure 5.

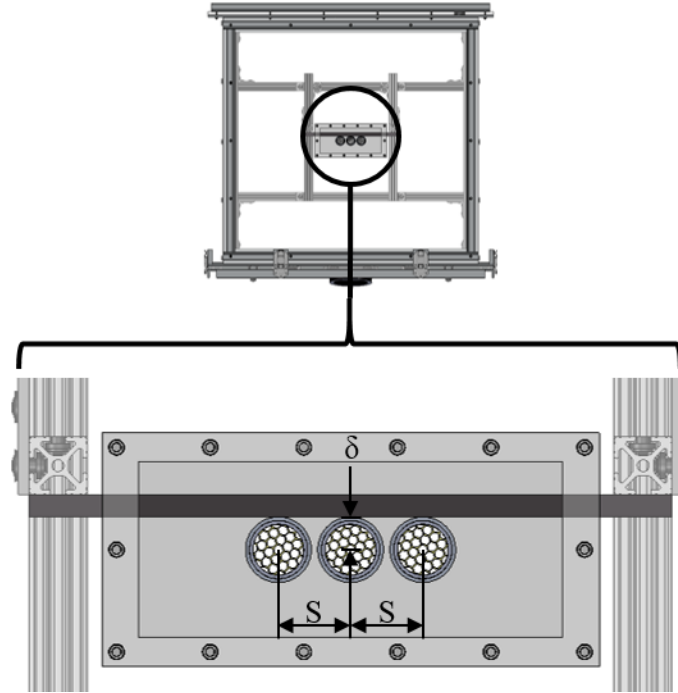


Figure 5: Top view of triple jet test section and confining wall with highlighted spacing parameters

The outlet velocities of the individual jets were determined according to their corresponding volumetric flow rates (governed by the automated valves) and the diameter of the jets. The Reynold's numbers for the jet outlets were calculated based on these velocities and the corresponding temperature dependent fluid properties as a function of the jet outlet temperatures. With the jet outlet velocities and temperatures known, the velocity ratio and temperature difference are calculated with ease. The test cases are presented in Table 1.

Table 1: Experimental conditions

Case name	Hot jet			Cold jet (center)			R	ΔT (°C)	δ
	V_H (m/s)	Re_H	T_H (°C)	V_C (m/s)	Re_C	T_C (°C)			
Case 1	15.63	1.79×10^4	62.1	7.75	1.07×10^4	28.8	0.50	33.3	0.5
Case 2	7.75	8.88×10^3	61.6	7.75	1.08×10^4	28.2	1.00	33.4	0.5
Case 3	5.12	5.89×10^3	61.1	7.75	1.08×10^4	27.5	1.51	33.6	0.5
Case 4	15.63	1.67×10^4	75.8	7.75	1.05×10^4	31.3	0.50	44.5	0.5
Case 5	7.75	8.24×10^3	76.8	7.75	1.05×10^4	32.0	1.00	44.8	0.5
Case 6	5.12	5.51×10^3	74.2	7.75	1.07×10^4	29.5	1.51	44.7	0.5
Case 7	15.63	1.76×10^4	65.6	7.75	1.05×10^4	32.7	0.50	32.9	1.0
Case 8	7.75	8.76×10^3	64.4	7.75	1.06×10^4	31.0	1.00	33.4	1.0
Case 9	5.12	5.86×10^3	61.9	7.75	1.07×10^4	28.4	1.51	33.4	1.0
Case 10	15.63	1.63×10^4	80.4	7.75	1.03×10^4	36.2	0.50	44.3	1.0
Case 11	7.75	8.18×10^3	78.2	7.75	1.04×10^4	33.8	1.00	44.3	1.0
Case 12	5.12	5.47×10^3	75.7	7.75	1.05×10^4	31.3	1.51	44.4	1.0

For convenience, the velocity ratio, R will be referred to in terms of its nominal value for the analysis to follow, i.e. $R \approx 0.5, 1.0, \text{ or } 1.5$. Several non-dimensional parameters are incorporated as well. The non-dimensional axial direction X^* is defined as

$$X^* = \frac{X}{D} \quad (3)$$

Where X is the downstream distance from the outlet of the cold jet and D is the diameter of an individual jet. The non-dimensional radial direction Y^* is defined as

$$Y^* = \frac{Y}{S} \quad (4)$$

Where Y is the inline distance along the jet outlets from the cold jet center and S is the jet spacing as seen previously in Figure 5. A visual representation of the non-dimensionalized directions X^* and Y^* is found in Figure 6.

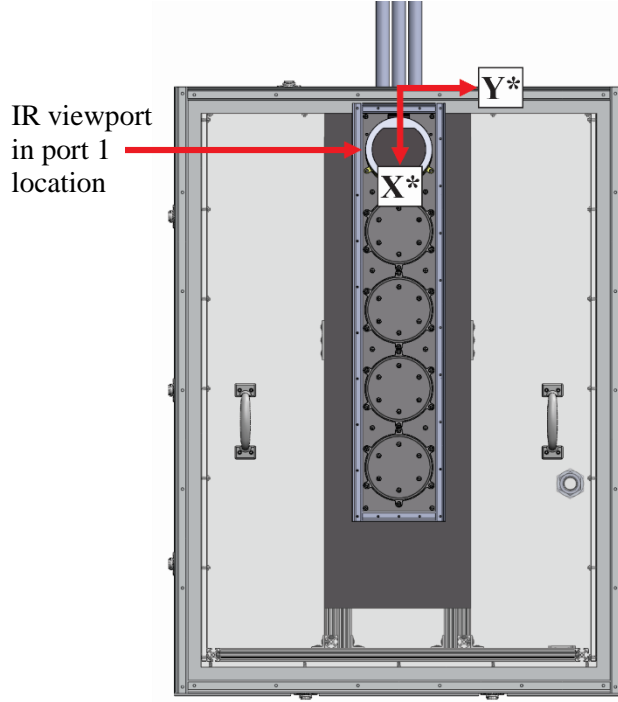


Figure 6: Front view of test section and IR viewports with non-dimensional axial directions highlighted

Additionally, for direct comparison of the temperature profiles found on the polycarbonate plate for each test case, the temperature on the plate is non-dimensionalized according to Equation (5).

$$\theta = \frac{T_i - T_C}{T_H - T_C} \quad (5)$$

Where T_i is the local surface temperature at an individual point (pixel) as measured by the IR camera. The non-dimensional temperature (θ) ensures that any differences in jet outlet temperature between test cases are accounted for in direct comparisons between the cases provided in Table 1.

2.3 EXPERIMENTAL METHODS

The jet outlet temperatures are determined experimentally by placing a type-T thermocouple at the outlet of each jet. It is assumed that the thermocouples are sufficiently small such that they did not interfere with the velocity profiles at the outlet of the jets. The thermocouples were calibrated using an OMEGA hot point® Dry Block Probe Calibrator and reference thermistor with an accuracy of ± 0.156 °C at a maximum operating temperature of 130 °C. A FLIR SC5000 IR camera with a resolution of ± 1.0 °C for absolute temperatures is used to acquire the temperature signatures induced by the jets on the parallel plate. The IR camera was calibrated with a blackbody emitter (Infrared Systems Development model IR-2106 radiation source and model IR-301 digital temperature controller) with an accuracy of ± 0.2 °C at a maximum operating temperature of 150 °C. The accuracy of the measurement equipment is incorporated into the overall uncertainty in θ , and is evaluated in Section 3.2.

The test section walls are composed of 1.11 cm thick polycarbonate and have poor infrared transmittance in the wavelength spectrum of the IR camera (2.1-5.1 μm). For this reason, a FLIR 4-inch Infrared (IR) viewport (model IRW-4C) is incorporated, which includes a broadband crystal lens with a maximum operating temperature of 260°C. The camera is placed 55.88 cm from the front surface of the parallel plate enabling a resolution of 0.5 mm. To avoid reflection of the camera on the IR window, a custom mount is built which ensures that the window axis and camera axis are offset by 10°. Additionally, a shroud is placed between the camera lens and the viewport which eliminates any incident thermal radiation. Accommodation exists for 5 viewports on the front surface of the test section with a center-to-center distance of 15.24 cm for each adjacent viewport. The angled mount and IR window can be placed in any of these five viewports with the remaining

viewports sealed with plugs. Each viewport allows for a perspective of the parallel plate with an image approximately 7.7 jet diameters in height, and 6.0 jet diameters in width of the parallel plate. The viewport design is represented in Figure 6. For the current study, the three preeminent regions of flow (entrance, convective mixing, and post mixing) are all observable in the first three viewports for every experimental case. For these three viewports a downstream distance up to $X^* = 21.46$ and $X^* = 21.60$ can be observed for the cases utilizing a plate spacing of $\delta = 0.5$ and $\delta = 1.0$, respectively. It is assumed that as far as $X^* = 20$, there are no edge effects from the tank, such that it is sufficiently large to accommodate the flow phenomena of the jets on the plate without interference. Some amount of overlap exists between images captured at neighboring viewports such that a continuous domain can be obtained when stitching together the infrared measurements. For the spacing $\delta = 0.5$, the overlap between viewports 1 and 2 was $1.02D$ and for viewports 2 and 3 was $0.76D$. For the spacing $\delta = 1.0$, the overlap between viewports 1 and 2 was $1.33D$ and for viewports 2 and 3 was $1.08D$.

3.0 RESULTS

3.1 TEMPERATURE PROFILE CASE STUDY

The temperature profiles captured by the IR camera for cases 4-6 in Table 1 are presented in Figure 7. Cases included in Figure 7 are selected for having the highest temperature difference ($\Delta T = 44.4^\circ\text{C}$) at the closest plate spacing ($\delta = 0.5$) and therefore reveal the highest temperature contrasts, and most easily illustrate the mixing patterns. The temperature scaling of each figure is held constant to enable qualitative and quantitative comparisons between experimental images.

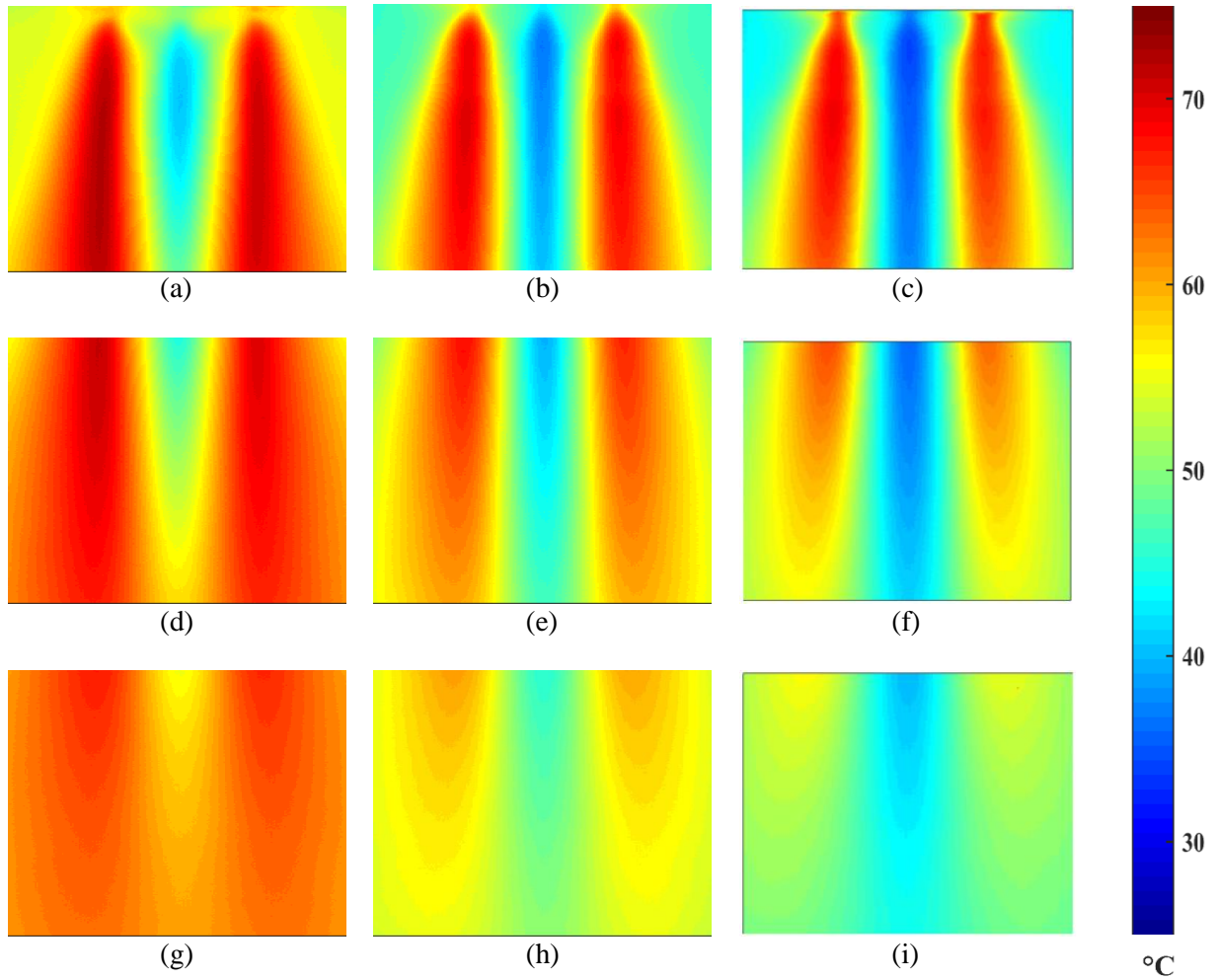


Figure 7: Contours of triple jet-induced temperature fields across parallel wall for $\Delta T = 44.4\text{C}$ and $\delta = 0.5$. Approximate size of each image is 13.4 cm x 17.1 cm (a) $R = 0.5$ port 1 (b) $R = 1.0$ port 1 (c) $R = 1.5$ port 1 (d) $R = 0.5$ port 2 (e) $R = 1.0$ port 2 (f) $R = 1.5$ port 2 (g) $R = 0.5$ port 3 (h) $R = 1.0$ port 3 (i) $R = 1.5$ port 3

It should be noted that the other case studies provided similar contours and are therefore omitted, but the data are included in the analysis that follows. From Figure 7, the most visible influence of the unique jet outlet temperatures on the surface temperature of the polycarbonate plate is in the $R = 1.5$ port 1 temperature field (Figure 7 (c)). The results show the presence of the jets is immediately felt by the plate with high temperature contrasts near the jet nozzles. This region, where negligible change in temperature has occurred, is considered the entrance region,

and can be observed in the port 1 location for all three velocity ratios (Figure 7 (a) through (c)). The impact of the velocity ratio itself can most easily be viewed by comparing these three thermal maps. For the $R = 0.5$ port 1 image (Figure 7 (a)), the hot jets dominate the temperature profile seen on the plate and the presence of the central cold jet is quickly ‘washed out’. The $R = 0.5$ condition requires the highest relative hot jet velocities of all of three proposed velocity ratios and therefore induces turbulent mixing the furthest upstream as is evident in Figure 7 (d), in which the hot jets entrain the most fluid from the center cold jet, ‘washing out’ the cold jet further upstream as compared to Figure 7 (e) and (f). Recall that as referenced in Table 1, the center cold jet velocity (and therefore volumetric flow) is fixed for all cases. This phenomena is characteristic of the convective mixing region, which becomes more apparent with increasing downstream distance in Figure 7 (d) and (g). While the momentum of the hot jets still dominates the spreading of the temperature profile on the plate, the effects are hindered by the increase in fluid mass downstream as well as the apparent thermal mixing. By the lower half of port 3 in Figure 7 (g), the profile is in the post mixing regime with visibly near uniform temperatures across the surface of the plate.

In the $R = 1.0$ (isovelocity) images (Figure 7 (b), (e), (h)), the cold jet’s influence on the thermal field seen on the plate is apparent in all three port locations. This is due to the isovelocity condition itself, in which the mixing of the three jets are visibly delayed further downstream. Therefore, for the $R = 1.0$ condition in Figure 7, the convective mixing of the jets is now based primarily on the temperature difference between the jets since there is negligible difference in velocity between the center and outer hot jets. While the post mixing region appears prominently in $R = 0.5$ port 3 (Figure 7 (g)), it is unclear whether sufficient mixing has occurred to label $R = 1.0$ port 3 (Figure 7 (h)) as being in the post mixing region, as the thermal influence of all three

jets are clearly still visible. It is evident that the isovelocity condition is inhibiting thermal mixing on the plate surface further downstream in comparison to the $R = 0.5$ thermal fields.

In the $R = 1.5$ images (Figure 7 (c), (f), (i)), the cold jet velocity is sufficiently higher than the two adjacent hot jets' velocities such that the cold jet dominates the temperature field seen on the plate. Thus, the cold jet is instead beginning to "push out" the adjacent hot jets in port 2 in the convective mixing region. Interestingly, the thermal mixing behavior seen towards the bottom of the $R = 1.5$ port 3 image seems well mixed, as there is little delineation of the three jets, yet the influence of the cold jet is still prominent in the top half of port 3. By comparison of the contrast of each temperature, $R = 0.5$ port 3 image appears to have a smaller difference in temperature than that of $R = 1.5$ port 3. This observation stands with the previous conclusion that higher outlet velocities (such as those required for the $R = 0.5$ condition as compared to the $R = 1.5$ condition) promote thermal mixing further upstream.

These nine plots in Figure 7 provide a comprehensive example of the three mixing regions for round jets, similar to the example identified in a previous slot jet study by Kimura et al. [11], provided as a reference in Figure 8.

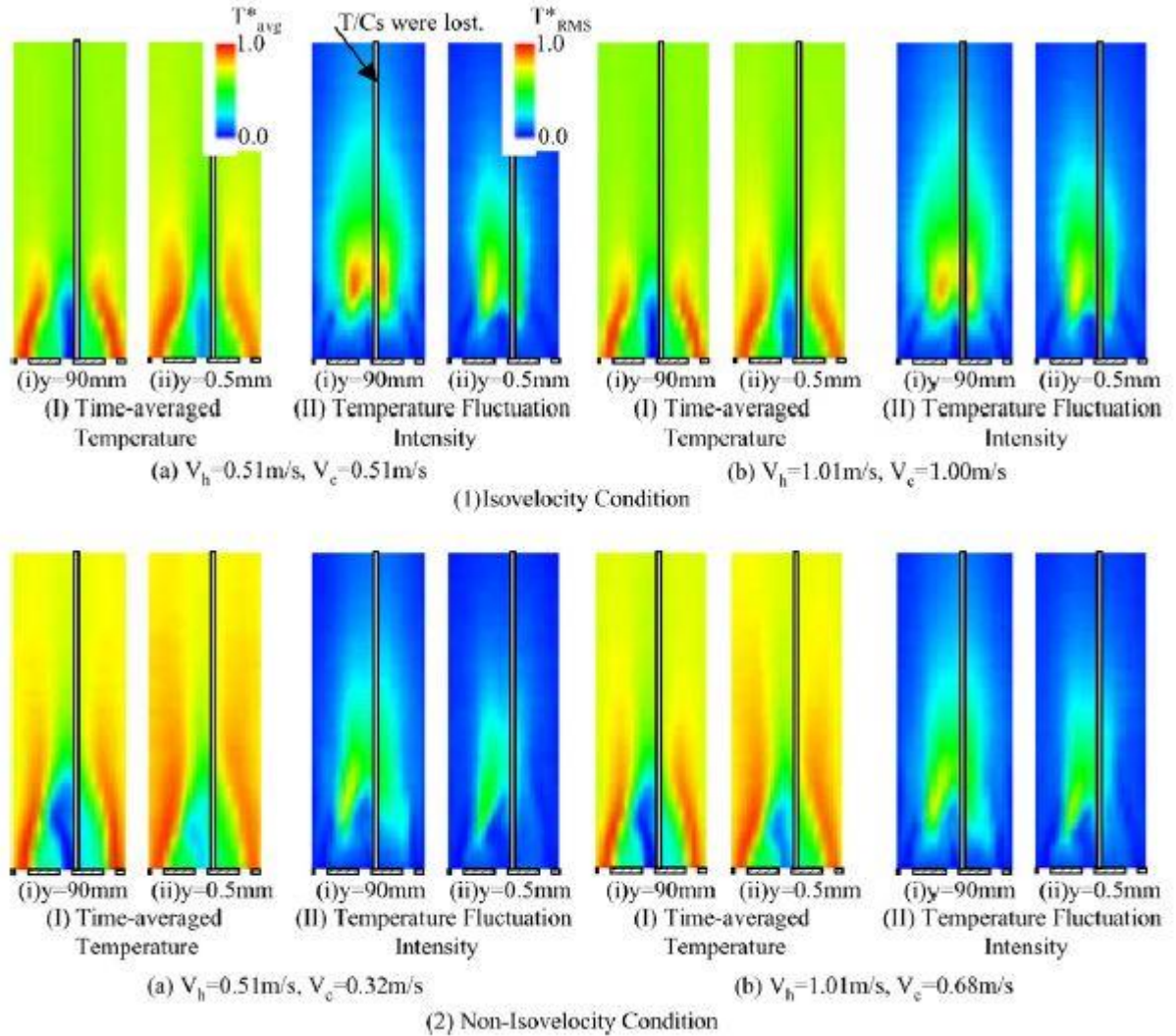


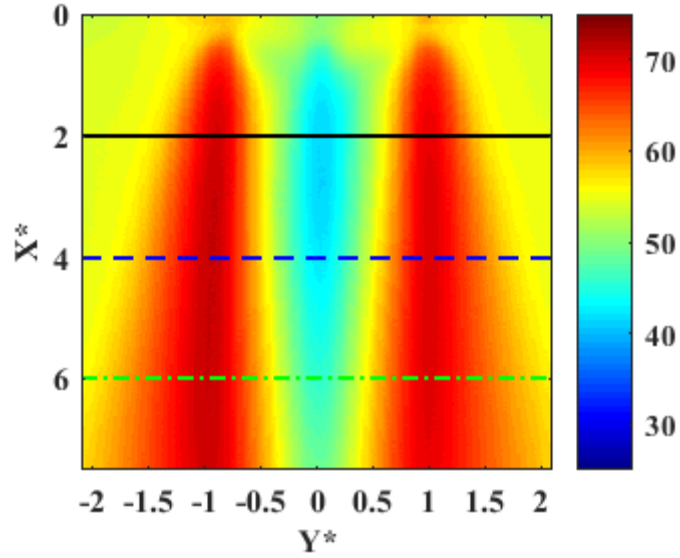
Figure 8: Time-averaged temperature contours and corresponding temperature fluctuations from Kimura et al. [11]

This previous study utilized a similar triple slot jet configuration with a jet center-to-center spacing of $S = 7.0$ cm (over twice as large as $S = 3.13$ cm, the spacing used in the current study) sandwiched between two parallel walls using liquid sodium. Fluid contours were produced using a thermocouple tree that was mounted in a near wall position and in the midposition between the two walls of the three slot jets. The slot jet cases consisted of considerably higher absolute temperatures with liquid sodium as the working fluid, but almost near identical temperature

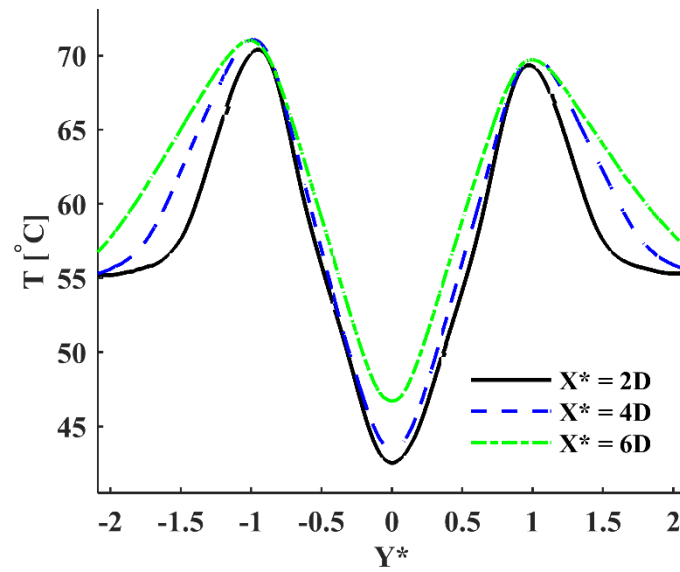
differences between the jets [11]. The use of water and air as substitutes for liquid sodium has been outlined by Moriya and Ohshima [30] for simulating the characteristics of temperature fluctuation due to turbulent mixing. Since the contours provided by Kimura et al. are time-averaged, their qualitative comparison to the steady-state contours provided in Figure 7 is justified. The geometry of the slot and round jet outlets induce different thermal profiles in the entrance region, however the majority of the difference in the downstream mixing is attributed to the spacing between the jets being more than double that of the current study. The contours of the round jets' thermal interactions with the surface of the plate show much wider spreading in the Y^* -direction in contrast to the relatively narrow and more distinct shape seen by the fluid interactions of the slot jets.

3.2 TEMPERATURE LINE TRACE COMPARISON

Line traces of the temperature data were utilized in $X^* = 2$ increments in the downstream X^* -direction for each temperature field. A total of 10 line traces were evaluated accounting for a range of X^* values between $X^* = 2$ -20 downstream. As an example, a visualization of the line traces and the corresponding temperatures are provided in Figure 9 for port 1 of case 4.



(a)



(b)

Figure 9: (a) Case 4, port 1 temperature field with imposed line traces (b) Case 4, port 1 polycarbonate plate line trace surface temperatures

The line traces provide an array of temperatures along the width of the plate, in the Y^* -direction. For an improved understanding of the characteristic behavior of the line traces, the asymmetry of each trace was resolved by averaging each line trace about its center-most point, the

cold jet center. The relative asymmetric error, ϵ_{asym} for two individual symmetrically averaged pixels was found according to Equation (6).

$$\epsilon_{asym} = \frac{|\theta_{LHS} - \bar{\theta}|}{\bar{\theta}} \quad (6)$$

Where θ_{LHS} is the non-dimensionalized temperature at the left hand side pixel location and $\bar{\theta}$ is the average between θ_{LHS} and θ_{RHS} , the symmetric non-dimensionalized temperature on the right hand side. The maximum relative asymmetric error for a single pixel in each case was found according to Equation 6 and all values are presented in Table 2.

Table 2: Maximum average asymmetric error across all line traces for each case

Case Name	Maximum Relative Asymmetric Error (ϵ_{asym})
Case 1	3.27%
Case 2	3.70%
Case 3	4.32%
Case 4	6.13%
Case 5	2.99%
Case 6	4.17%
Case 7	4.93%
Case 8	3.78%
Case 9	4.35%
Case 10	2.98%
Case 11	3.01%
Case 12	3.88%

The average relative asymmetric error for all cases was found to be $\epsilon_{asym} = 3.96\%$ with a maximum error of 6.13% for case 4. Therefore, averaging the two profiles and using that result for subsequent analysis is warranted.

Since the averaged dimensionless profiles are used as metrics of interest in this study, the experimental uncertainty for these values must also be determined. In order to address this, case 4 is used as a bounding scenario since it experiences the highest temperature difference at the highest velocity of each jet. The plate spacing of $\delta = 0.5$ is arbitrary for this analysis. To determine

repeatability, a total of five tests with these identical experimental settings were run over the course of 10 days. Although the temperature of the room was found to fluctuate throughout the day, which caused some amount of variation in absolute temperatures, the dimensionless form of the temperature was found to show excellent repeatability from day to day. The repeatability error in this case is quantified using the standard deviation between the tests as defined in Equation (7).

$$S_{\theta,T} = \sqrt{\frac{\sum_{i=1}^{N=5} (T_i - \bar{T})^2}{v}} \quad (7)$$

Where $N = 5$ in accordance with the 5 total sets of measurements of the plate surface temperature gathered for the repeatability study. A precision interval is incorporated in the repeatability uncertainty according to the student's t distribution, $t_{v,P}$, such that a given measurement should be within this interval to 95% confidence. The uncertainty in repeatability ($U_{\theta,R}$) is given by Equation (8).

$$U_{\theta,R} = t_{v,P} \frac{S_{\theta,T}}{\sqrt{N}} \quad (8)$$

This uncertainty in repeatability is found for every pixel value of every line trace. It is important to note that the sensors themselves also introduce uncertainty. The uncertainty in a given value for θ is a function of the uncertainty in the individual temperature measurements. Type-T thermocouples were used to determine T_C and T_H as referenced in the definition of θ provided by Equation (5). The cold jet outlet temperature, T_C , incorporates the uncertainty in the resolution of the type T-thermocouples and the uncertainty in the calibration of the cold jet thermocouple according to a seventh order polynomial curve fit. The hot jet temperature, T_H , includes the same uncertainty in the resolution of the type T-thermocouples and uses the higher uncertainty in the calibration of the two hot jet thermocouple's seventh order polynomial curve fit, for a conservative

calculation of the uncertainty. The total uncertainty in precision for each thermocouple is calculated according to Equation (9).

$$U_{T_H} = \sqrt{U_{T_H,res}^2 + U_{T_H,cal}^2} \quad (9)$$

Note that in Equation (9), the subscript “ T_H ” is used for convenience. An identical approach is made for the cold jet thermocouple replacing “ T_H ” with “ T_C ” in Equation (9). The IR camera was used to find T_i according to Eqn. (5) at each discrete pixel for each line trace in the current study. The total uncertainty in precision of the IR camera included the resolution of the IR camera and the calibration procedure as previously mentioned in Section 2.3. The total uncertainty in precision of the IR camera is calculated according to Equation (10).

$$U_{T_i} = \sqrt{U_{T_i,res}^2 + U_{T_i,cal}^2} \quad (10)$$

With the repeatability in total uncertainty in each measurement device known, the precision uncertainty in the non-dimensional temperature ($U_{\theta,P}$) is found using standard error propagation analysis [31].

$$U_{\theta,P} = \sqrt{\left(\frac{\partial\theta}{\partial T} \cdot U_{T_i}\right)^2 + \left(\frac{\partial\theta}{\partial T_H} \cdot U_{T_H}\right)^2 + \left(\frac{\partial\theta}{\partial T_C} \cdot U_{T_C}\right)^2} \quad (11)$$

Combining the uncertainty in precision with that of the repeatability in a standard fashion (i.e., square root of the sum of squares), yields the total uncertainty in θ for a single pixel in the IR image and is defined explicitly in Equation (12).

$$U_{\theta,TOT} = \sqrt{U_{\theta,P}^2 + U_{\theta,R}^2} \quad (12)$$

As an example, the uncertainty analysis is applied to the case 4 line traces with the results provided in Table 3 for the geometric jet centerline locations at incremental X^* downstream distances.

Table 3: Total uncertainty in non-dimensionalized temperature for case 4

X^*	Uncertainty in non-dimensional temperature, $U_{\theta,TOT}$		
	Hot Jet Center ($Y^* = -1$)	Cold Jet Center ($Y^* = 0$)	Hot Jet Center ($Y^* = 1$)
2	+/-0.043	+/-0.037	+/-0.043
4	+/-0.040	+/-0.037	+/-0.040
6	+/-0.039	+/-0.034	+/-0.039
8	+/-0.040	+/-0.034	+/-0.040
10	+/-0.038	+/-0.034	+/-0.038
12	+/-0.036	+/-0.035	+/-0.036
14	+/-0.035	+/-0.034	+/-0.035
16	+/-0.034	+/-0.035	+/-0.034
18	+/-0.034	+/-0.035	+/-0.034
20	+/-0.033	+/-0.035	+/-0.033

As can be seen from Table 3, the uncertainty is highest at the jet outlets and then decreases with distance downstream, although this change is quite mild. For the $X^* = 2$ line trace, the majority of the uncertainty is due to the resolution of the measurement instrumentation ($U_{\theta,P} = 0.032$ for the left hot jet, $U_{\theta,P} = 0.033$ for the cold jet, and $U_{\theta,P} = 0.032$ for the right hot jet). For these same locations, the repeatability errors are $U_{\theta,R} = 0.028$ for the left hot jet, $U_{\theta,R} = 0.018$ for the cold jet, and $U_{\theta,R} = 0.028$ for the right hot jet. The uncertainty range for every third point along the $X^*=2$ line temperature trace can be seen in Figure 10. For consistency, the symmetrically averaged line temperature trace is displayed with the corresponding symmetrically averaged uncertainty bars. Therefore, the uncertainty bars in this plot are the average between the left side ($Y^* < 0$) and right side ($Y^* > 0$) values.

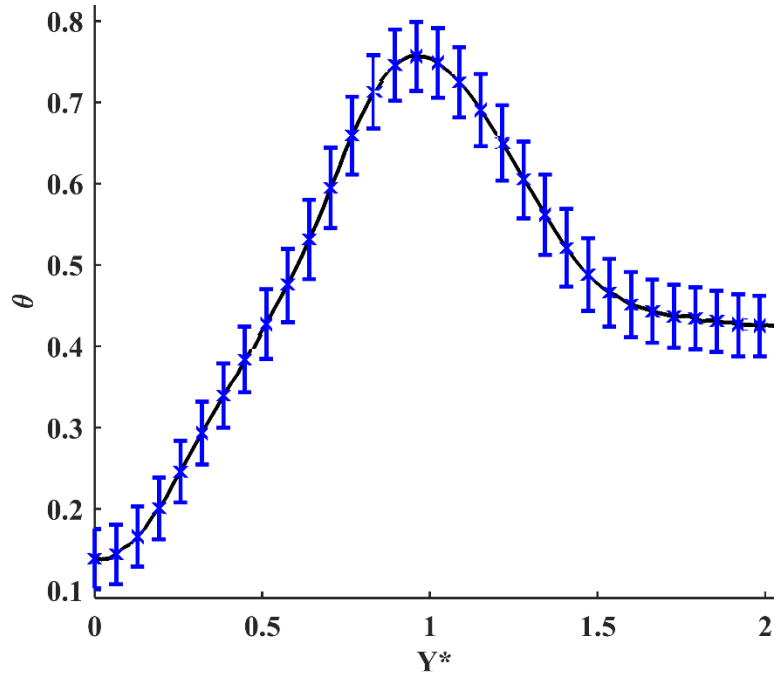
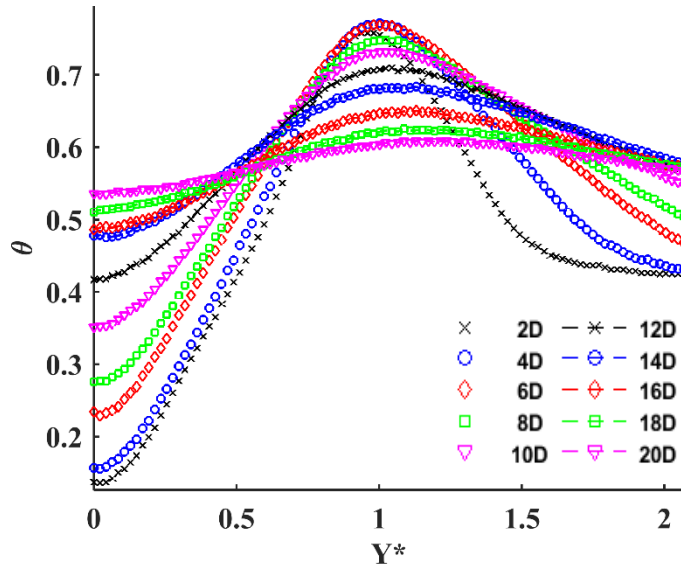
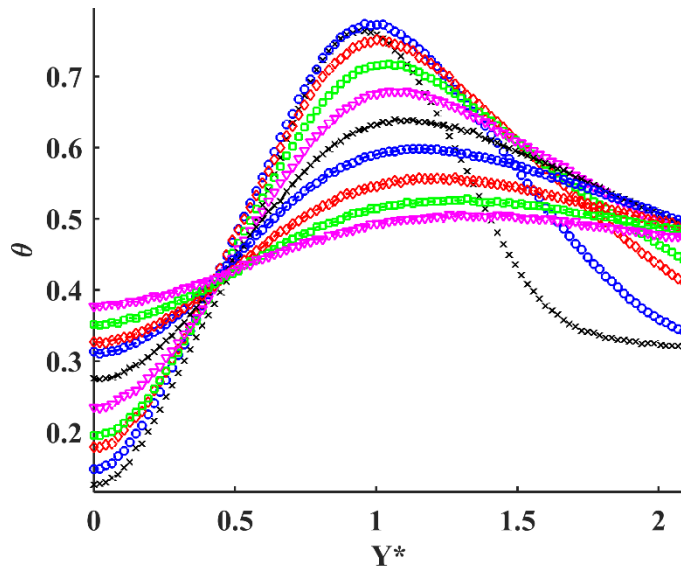


Figure 10: Total uncertainty range for $X^*=2$ line trace of case 4

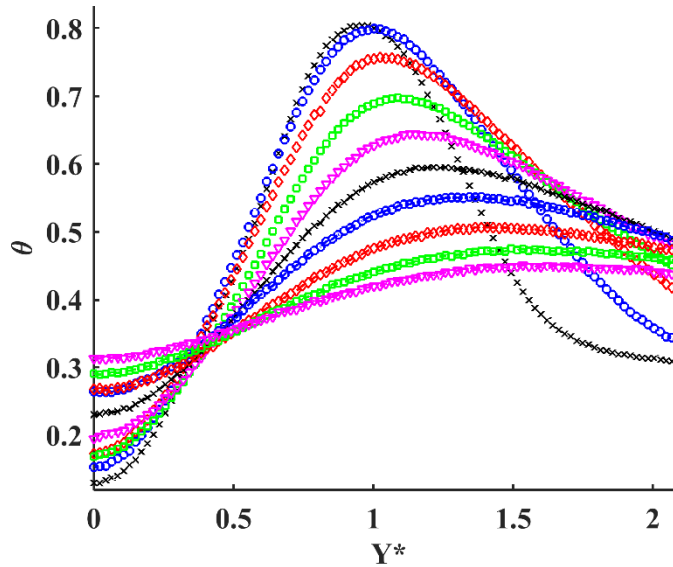
As seen in Figure 10, the magnitude of the uncertainty bars are roughly equal across the entirety of the line temperature trace with a minimum of $U_{\theta, TOT} = 0.036$ and maximum of $U_{\theta, TOT} = 0.053$. With symmetrically averaged profiles justified and the worst case uncertainty now quantified, the analysis henceforth includes only half of a given profile, to eliminate redundancy about the center in the Y^* -direction. A family of line temperature profiles between $X^* = 2$ and 20 are shown in Figure 11 for the three velocity ratios at $\Delta T = 44.4^\circ\text{C}$ and $\delta = 0.5$.



(a) Case 4: $R = 0.5$



(b) Case 5: $R = 1.0$



(c) Case 6: $R = 1.5$

Figure 11: Line temperature profiles with fixed $\Delta T = 44.4^\circ\text{C}$ and $\delta = 0.5$

For these dimensionless temperature profiles, the values are bounded between 0 (when $T = T_C$) and 1 (when $T = T_H$). It is interesting to note that in all three plots of Figure 11, the values at the center of the cold and hot jets are distanced from these extreme bounds, even for the $X^* = 2$ curve (only 2 diameters downstream). At the center of the cold jet ($Y^* = 0$), the minimum values are between 0.1 and 0.15, while near the center of the hot jet ($Y^* = 1$), the maximum values are near 0.8. This difference can be explained by two factors. First, each jet has a non-uniform temperature profile, and T_C and T_H represent the centermost temperature of the cold and hot jets, respectively. Therefore, the temperatures seen on the plate (near the edge of the jet) will tend toward the average of T_C and T_H . Additionally, the energy exchange between neighboring jets (as well as that of the surrounding air in the large enclosure, which is somewhere between T_C and T_H) causes the temperatures to drift toward the average value. Generally speaking, the temperature profiles become increasingly uniform with downstream distance in the X^* -direction implying that the

temperature profile on the plate is becoming more evenly mixed. Although this is true for all three plots in Figure 11, the impact of R is easily seen when comparing the value of θ for the profile closest to the fully mixed condition ($X^* = 20$). In Figure 11(a), where $R = 0.5$, the variation of temperature at $X^* = 20$ is bounded between $0.54 < \theta < 0.61$, while for $R = 1.0$ (Figure 11(b)) these bounds are between 0.38 and 0.51. When the cold jet velocity is highest ($R = 1.5$, Figure 11(c)), these bounds naturally decrease further ($0.31 < \theta < 0.45$). This behavior is qualitatively in line with what one would expect for mixing of the two non-isothermal streams. If the settings listed in Table 1 were applied to an analogous internal flow scenario, one could easily apply a mass energy balance and predict the fully mixed temperatures. For the conditions employed in Figure 11, this would suggest fully mixed dimensionless temperatures of 0.66, 0.52, and 0.42 for Figure 11(a), (b), and (c), respectively. This implies that the upper limits of the $X^* = 20$ non-dimensional temperature profiles for each of the cases in Figure 11 are in good agreement with the theoretical fully mixed temperatures from a mass energy balance perspective.

A conservative approach to defining a “uniformly mixed” profile would be the expectation that sufficiently far downstream, and with no outside influence, the temperature profile will become horizontal, such that for that profile, θ is a constant value such as those values proposed by the mass energy balance analysis above. Interestingly, for the $X^* = 20$ line trace, the average value of θ ($\bar{\theta}$) and the maximum difference in values of θ across the line trace are $\bar{\theta} = 0.58, 0.46, 0.40$ and $\Delta\theta_{X^*=20} = 0.07, 0.13, 0.14$ for Figure 11(a), (b), and (c), respectively. This implies that with decreasing velocity ratios, R , the average non-dimensional temperature, $\bar{\theta}$, far downstream increases yet the range in horizontal values of θ decreases. While a formal definition of the “amount” of thermal mixing taking place on the plate surface is debatable, it is clear that the

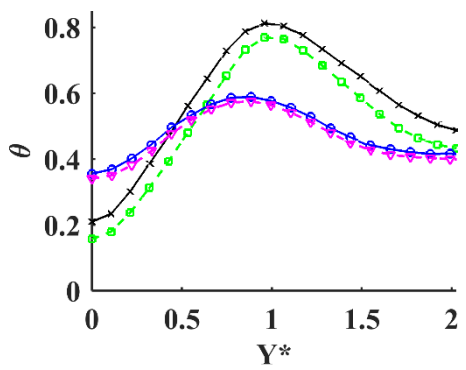
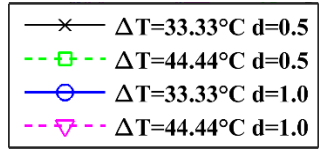
decreasing values of velocity ratio promote uniformity in horizontal surface temperatures for the test cases of Figure 11.

The $R = 0.5$ condition as seen in Figure 11(a) displays the dominance of the hot jets on the surface of the plate and the influence on the thermal mixing with increasing downstream distance. The “washing out” of the cold jet previously alluded to in Section 3.1 is here quantitatively evaluated as the aggressive shift in the non-dimensional surface temperature along $Y^* = 0$ (the cold jet geometric center) with increasing downstream distance. At $X^* = 2$ the cold jet centerline non-dimensional temperature is $\theta = 0.14$ and at $X^* = 20$, is $\theta = 0.54$, accounting for an increase of $\Delta\theta = 0.40$. This shift in surface temperature across the $2 < X^* < 20$ region of the plate is much larger when compared to the $R = 1.0$ and $R = 1.5$ conditions in Figure 11(b) and (c) which have shifts of $\Delta\theta = 0.25$ and $\Delta\theta = 0.18$, respectively. The same aggressive shift in surface temperature can be seen around the hot jet center line $Y^* = 1$, for the $R = 1.5$ condition of Figure 11(c) in which the non-dimensional temperature at $X^* = 2$ is $\theta = 0.80$ and at $X^* = 20$ is $\theta = 0.45$, accounting for a of $\Delta\theta = -0.35$. The shift in surface temperature around $Y^* = 1$, is significantly larger than those of $R = 0.5$ in Figure 11(a) and $R = 1.0$ in Figure 11(b), of which were $\theta = -0.15$ and $\theta = -0.26$, respectively. While the downstream shift in surface temperature across the hot jet center line in the $R = 1.5$ condition is significant, it is not nearly as severe as that of the shift across the cold jet centerline in the $R = 0.5$ condition. This is attributed to the increased turbulence provided by the $R = 0.5$ condition in case 4, in which all three jets operate at their maximum velocities relative to all of the proposed test cases (as seen in Table 1). Recall that the cold jet velocity is fixed for all of the proposed test cases, and therefore, the $R = 1.5$ condition has the cold jet operating at a similar Reynolds number as all other cases, with the hot jets flowing at two-thirds the flow rate of the

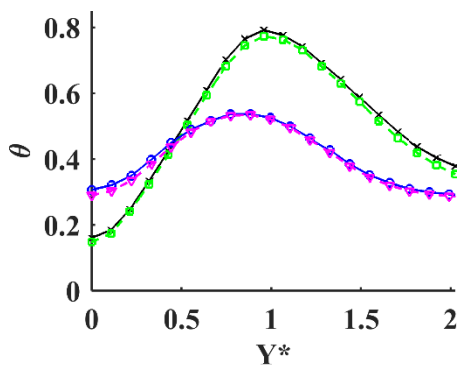
center cold jet, implying that the hot jets operate at much lower Reynolds numbers compared to case 4.

More recent numerical work [8] involving a similar parallel triple slot jet configuration with all isovelocity cases has suggested that with increasing Reynolds number, the mixing of hot and cold fluid is delayed and the area of the convective mixing region is increased. A more important fundamental understanding of the effect of the Reynolds number of the jets on the induced convective mixing involves the present comparison of the non-isovelocity cases to an isovelocity case at a fixed temperature difference. From the current analysis it is clear that the $R=0.5$ condition, which includes the largest Reynolds numbers out of the three velocity ratios, reaches a more uniform temperature across the Y^* direction of the plate further upstream than that of the $R = 1.0$ or $R = 1.5$ cases. The same behavior is seen in more detail by comparing the three plots of Figure 11 with increasing downstream distance, the line traces of the temperature data for the $R = 0.5$ case reach a horizontal value more rapidly than either of the other velocity cases.

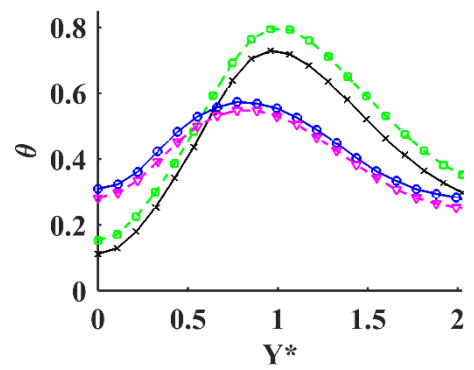
With the effect of the velocity ratio on the downstream temperature behavior understood, further comparisons are made to quantify the effect of temperature difference between the jets (ΔT) and the plate spacing (δ). This comparison is made by holding R constant, with results presented in Figure 12. Each plot in this figure is at a fixed R and X^* . The four curves represent line traces similar to those in Figure 11, but now consider each unique ΔT and δ combination. Three different X^* downstream distances are analyzed, corresponding to the three regions of flow: the entrance region ($X^* = 4$), the convective mixing region ($X^* = 14$), and the post-mixing region ($X^* = 20$), as found in the top, middle, and bottom rows, respectively, of Figure 12.



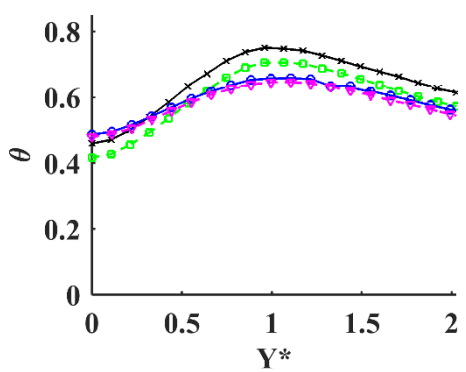
(a) $R = 0.5, X^* = 4$



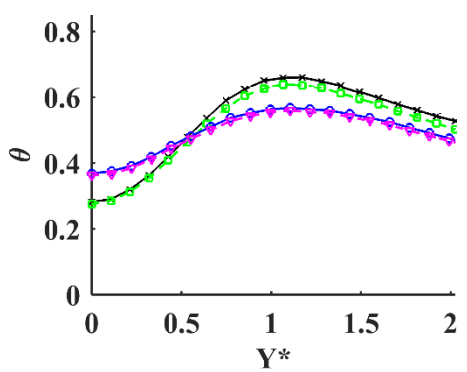
(b) $R = 1.0, X^* = 4$



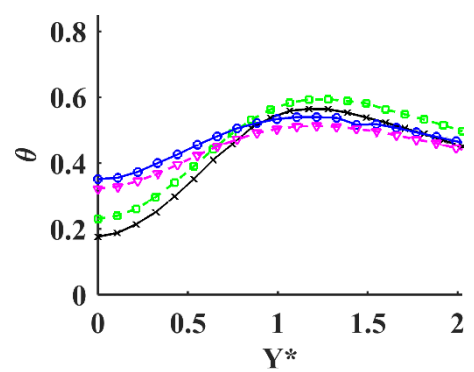
(c) $R = 1.5, X^* = 4$



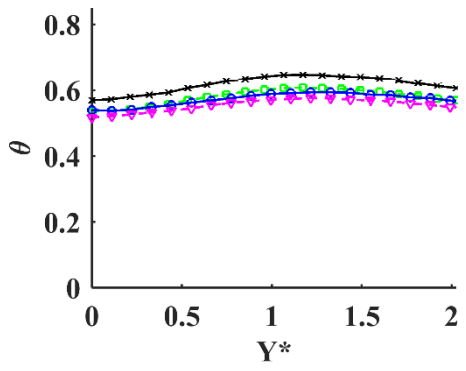
(d) $R = 0.5, X^* = 14$



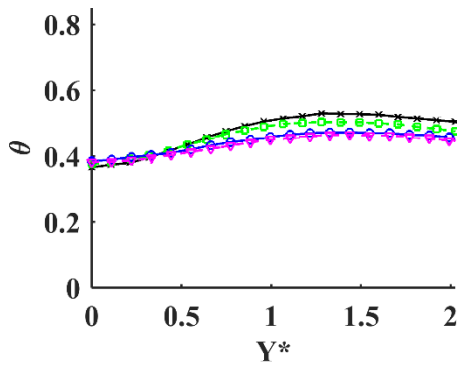
(e) $R = 1.0, X^* = 14$



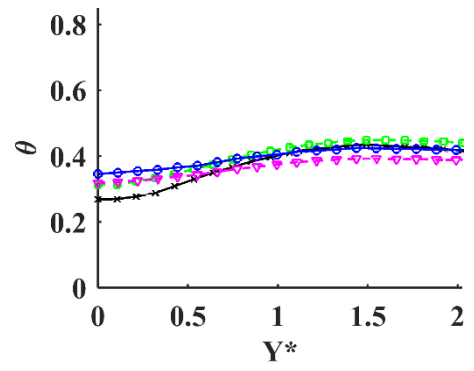
(f) $R = 1.5, X^* = 14$



(g) $R = 0.5, X^* = 20$



(h) $R = 1.0, X^* = 20$



(i) $R = 1.5, X^* = 20$

Figure 12: Temperature difference and plate spacing comparison in three characteristic flow regions

For each plot within Figure 12, the curves are grouped together. For the nearest downstream distance ($X^* = 4$, as provided in the top row), two distinct groupings are seen. It should be noted that $X^* = 4$ distance was chosen for the entrance region as opposed to the $X^* = 2$ trace, because for those cases utilizing a plate spacing of $\delta = 1.0$, the jets have not yet made marked contact with the plate. Figure 13 provides the temperature field for port 1 of case 10 with imposed line traces as an example. This image is used in direct comparison to case 4 in Figure 9(a) of which holds all variables in common with case 10 except that of the plate spacing ($\delta = 0.5$ and 1.0 for cases 4 and 10, respectively).

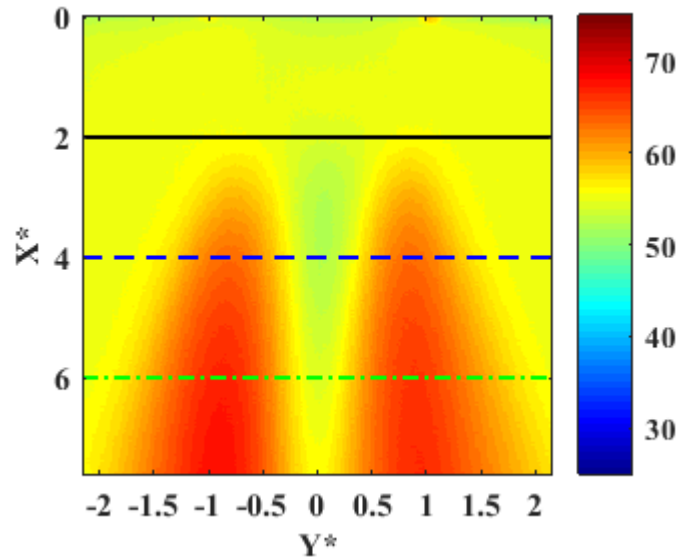


Figure 13: Case 10, port 1 temperature field with imposed line traces

The two curves with the highest peaks in Figure 12(a), (b), and (c) are those with $\delta = 0.5$, while the lower grouping are the curves from $\delta = 1.0$. This suggests the dimensionless temperature distributions on the plate are much more sensitive to δ and only slightly dependent on ΔT . This is not surprising, since one would intuitively expect that the location where the presence of the jets,

as first felt by the plate, would occur further downstream as δ increases. It is also interesting to compare the sets of curves for this top row between the three different velocity ratios. Taking the two $\delta = 0.5$ curves for Figure 12(a), (b) and (c), the change between them can easily be described by a slight vertical shift and a mild vertical scaling. The same could be said about the two $\delta = 1.0$ curves for each of the plots in the top row. Therefore, one could likely approximate the impact of R as a linear (slope plus intercept) shape function.

The same conclusions can be drawn for $X^* = 14$ (middle row of Figure 12), namely that two distinct groupings are seen, and can be described almost exclusively by δ , and R has the effect of introducing a shift and scaling of the line trace. Even further downstream at $X^* = 20$ (bottom row of Figure 12), the groupings are still present, but much less prominent. The vertical position, and to a much lesser extent at this location, the vertical scaling of the distribution are still dependent on R , but all four curves are roughly identical, irrespective of δ .

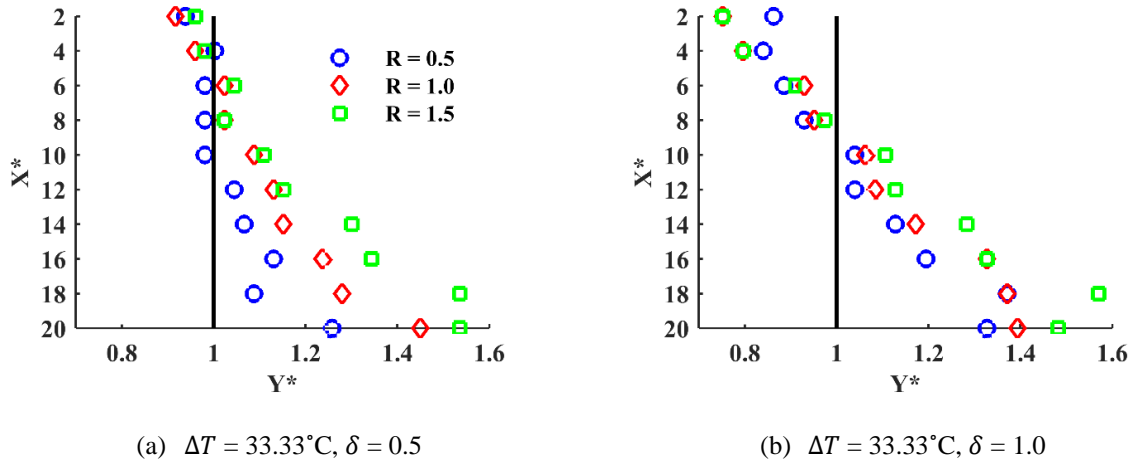
Since the behavior of the line trace is fundamentally the same shape, only shifted and scaled depending on R and/or δ , this suggests that with a modified dimensionless expression (one that accounts for shape factors), a generalized understanding is achievable and applicable across a wide range of operating conditions. Experiments including additional values for δ and R are needed to truly ascertain the likelihood of developing such a set of expressions.

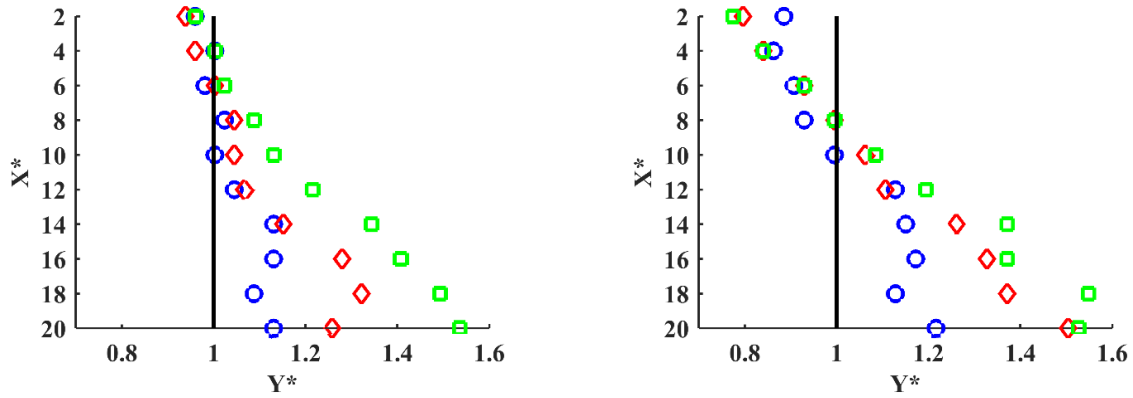
Previous experimental studies [6] involving a parallel triple slot jet configuration with the same hot-cold-hot configuration have noted that the majority of the convective mixing takes place at distances $X^* = 2.0 - 4.5$. Their experimental setup had significantly different variables including a jet center-to-center distance of $S = 7.0$ cm and temperature differences of 5°C and 10°C . The velocity ratios were $R = 0.5, 0.7,$ and 1.0 , with typical Reynolds numbers around 1.8×10^4 . While Figure 11 and Figure 12 show highlighted X^* distances downstream, the comparison of each

incremental X^* distance downstream done in the current study suggests that for the parallel round triple round jet configuration, the dominant convective mixing region occurs in the $8 < X^* < 16$ region. Interestingly, with a jet spacing approximately half as large as that used in the slot jet study and the differences in the jet outlet geometry considered, the convective mixing region is on the order of three times as large for the round jet observations as that of the slot jet study.

3.3 LOCATIONS OF MAXIMUM TEMPERATURE

The data contained in Figure 11 is analyzed in terms of the maximum temperature location and its variation as the flow travels downstream. This is provided in Figure 14, and is an indicator of the degree to which the hot jet veers away from the cold central jet.





(c) $\Delta T = 44.4^\circ\text{C}$, $\delta = 0.5$

(d) $\Delta T = 44.4^\circ\text{C}$, $\delta = 1.0$

Figure 14: Peak temperature location for each line temperature trace with imposed hot jet center line

The maximum temperature location directly below the outlets of the jet is, as expected fairly close regardless of R or ΔT . However the plate spacing clearly has an effect in the entrance region in that the average location in the $4 < X^* < 6$ range for the $\delta = 1.0$ spacing is closer to the center than that of the $\delta = 0.5$ spacing. Note that the $4 < X^* < 6$ region was chosen for this observation due to the jets' contact with the plate being delayed past $X^* = 2$ for the $\delta = 1.0$ spacing as previously noted in Figure 13. From Figure 14(a), along the $X^* = 4$ trace, the non-dimensional radial locations are $Y^* = 1.00, 0.96,$ and 0.98 for the $R = 0.5, 1.0, 1.5$ conditions, respectively and shows how tight these locations are around the hot jet axial center line. Figure 14(b) includes the same ΔT with the larger spacing, $\delta = 1.0$. The $X^* = 4$ line trace for this spacing yields $Y^* = 0.84, 0.80,$ and 0.80 for the $R = 0.5, 1.0,$ and 1.5 conditions, respectively. This shows that for all of the velocity ratios, the additional plate spacing causes a significant horizontal shift in the maximum surface temperature location on the plate. The same examination can be made by directly comparing Fig. 15(c) and (d) of which are held at the same $\Delta T = 44.4^\circ\text{C}$.

The effect of the velocity ratio R becomes much more apparent in the convective mixing region whose characteristic behavior begins in the $X^* \approx 8$ region. The maximum temperature

location spreads more sporadically in the Y^* direction with increasing values of R , and this behavior is consistent for each combination of ΔT and δ . For instance, in Figure 14(c) the location of the maximum temperature from the chosen initial location $X^* = 4$, to four times this distance downstream, $X^* = 16$, changes by a non-dimensional radial distance of $\Delta Y^* = 0.13, 0.32,$ and 0.41 for the $R = 0.5, 1.0,$ and 1.5 conditions, respectively. From similar inspection of the other plots of Figure 14, it is clear that the same conclusion can be drawn from each: with the velocity ratio R being the main variable driving thermal mixing in the convective mixing region, increasing values of R allow the influence of the cold jet to push out the hot jets. This in turn dissipates the influence of the hot jets on the plate, promoting thermal mixing of each hot jet separately with the cold jet, as opposed to the behavior of the $R = 0.5$ condition in which the opposite is true. By dissipating the influence of the cold jet on the plate, the maximum temperature on the surface of the plate should spread far less significantly, as is apparent with the much smaller ΔY^* in the region $4 < X^* < 16$.

As far as $X^* = 10$ downstream, the relative maximum temperature locations for a given case are fairly predictable, implying that the data could be explained through correlations. However, past the $X^* = 10$ mark, the locations for a given case become increasingly more sporadic. This observation provides support for the lower limit ($X^* < 16$) of the downstream range in the ΔY^* comparison above. The sporadic nature of the maximum temperature locations is explained in part by the convective mixing phenomena itself, however the increasing fluctuations further downstream are explained by the influence of the total mass entrained by the jets with increasing downstream distance. The increasing influence of the total mass and the significant decrease in momentum far downstream implies that the maximum temperature on the plate surface is subject to some fluctuation, as is characteristic of the post mixing region, and a trend line in this region is

no longer justified. This conclusion is in good standing with the observations made earlier in Section 3.2 regarding the uniform mixing far downstream in Figure 11 and justifies the transition area from the convective mixing region to the post mixing region as $X^* \approx 16$.

4.0 CONCLUSIONS

An experimental study of the interaction of three non-isothermal parallel round jets is conducted in a planar hot-cold-hot configuration. The jets are operated within the turbulent regime with a jet Reynolds number between 5.5×10^3 and 1.8×10^4 at three distinct cold to hot jet velocity ratios ($R = 0.50, 1.00, 1.51$). A flat polycarbonate plate is mounted parallel to the axial direction of the jets, and is offset in two different spacings: one half and one full jet diameter from the axial direction of the jets ($\delta = 0.5, 1.0$). The downstream thermal mixing of the jets are studied with temperature differences of $\Delta T = 33.33^\circ\text{C}$ and 44.4°C between the cold and hot jets. Steady-state results are captured via infrared thermography and indicate the thermal loading on the plate. The velocities of the individual jets are compared via the extreme velocity ratio cases $R = 0.50$ and 1.51 to that of the isovelocity case. The induced thermal line signatures on the plate surface suggest the most aggressive shifts in temperature occur in the area characteristic of the convective mixing region, defined here as the range $8 < X^* < 16$.

Qualitative thermal fields are analyzed with horizontal line traces of the plate surface temperature at downstream distances from the outlets of the jets in the range $2 < X^* < 20$. With a constant cold jet velocity for all cases, increasing hot jet velocities induce more turbulent mixing particularly in the convective mixing region promoting thermal mixing further upstream than that of the lower hot jet velocity cases. Interestingly, with increasing hot jet velocities, it is also found that while the average non-dimensional temperature far downstream ($X^* = 20$) increases, the range

in values across this thermal signature decreases. Far downstream mixing behavior is in good quantitative agreement with the fully mixed temperature expected from a mass energy balance approach.

By holding the velocity ratio constant, thermal signatures are also found to be highly dependent on the plate spacing and that the temperature differences considered in this study provided little influence. Results suggest the highest temperature differences on the surface of the plate occur in the plane common to the three jet axes. Additionally, for a give value of R , the thermal traces reach nearly identical values far downstream in the post mixing region, here defined as $X^* > 16$ regardless of plate spacing δ or temperature difference ΔT .

The peak temperature location on the surface of the plate at each downstream temperature trace is also of considerable interest in describing the overall shift in the transfer of heat across the surface of the plate. The maximum temperature location in the entrance region ($2 < X^* < 8$) is almost exclusively dependent on plate spacing δ with little influence from the velocity ratio R or temperature difference ΔT . In the $2 < X^* < 6$ range, the $\delta = 1.0$ spacing provides maximum temperatures closer to the axial center of the cold jet ($Y^* = 0$) than that of the $\delta = 0.5$ spacing. The effect of R becomes much more apparent in the convective mixing region where the maximum temperatures spread further in the Y^* -direction with increasing R , and this behavior is found to be consistent for each combination of ΔT and δ . The maximum temperature locations for a given case are found to be predictable as far as $X^* = 10$ downstream, but become increasingly more sporadic past this length. This is attributed to the increase in the total mass entrained by the jets and the decreasing influence of the momentum with increasing downstream distance.

This research represents preliminary predictions of the thermal loading in the VHTR lower plenum and provides validation data for fundamental and applied thermal mixing simulations.

With future verified computational analysis, the determination of the thermal loading as a function of the jet Reynolds numbers, the temperature difference between the jets, and the plate position can be found. These studies provide for useful insight in preventing thermal striping in the internal structural walls of the VHTR lower plenum and can be utilized in future work in material analysis of structural integrity in the VHTR core.

BIBLIOGRAPHY

- [1] P.E. MacDonald, P.D. Bayless, H.D. Gougar, R.L. Moore, A.M. Ougouag, R.L. Sant, J.W. Sterbentz, W.K. Terry, The Next Generation Nuclear Plant – Insights Gained from the INEEL Point Design Studies, in: Proceedings of the 2004 International Congress on Advances in Nuclear Power Plants (ICAPP '04), Pittsburgh, PA, USA, 2004.
- [2] S.B. Rodriguez, M.S. El-Genk, Numerical investigation of potential elimination of ‘hot streaking’ and stratification in the VHTR lower plenum using helicoid inserts, Nuclear Engineering and Design, 240(5) (2010) 995-1004.
- [3] C. Betts, C. Boorman, N. Sheriff, Thermal Striping in Liquid Cooled Fast Breeder Reactors, Thermal Hydraulics of Nuclear Reactors, (1983) 1292-1301.
- [4] A.M. Clayton, Thermal Shock in Nuclear Reactors, Progress in Nuclear Energy, 12(1) (1983) 57-83.
- [5] G.J. Lloyd, D.S. Wood, Fatigue Crack Initiation And Propagation as a Consequence of Thermal Striping, International Journal of Pressure Vessels and Piping, 8 (1980) 255-272.
- [6] A. Tokuhiro, N. Kimura, An experimental investigation on thermal striping mixing phenomena of a vertical non-buoyant jet with two adjacent buoyant jets as measured by ultrasound Doppler velocimetry, Nuclear Engineering and Design, 188 (1999) 49-73.
- [7] R.D. Blevins, Applied Fluid Dynamics Handbook, Van Nostrand Reinhold Co., New York, 1984.
- [8] Q. Cao, D. Lu, J. Lv, Numerical investigation on temperature fluctuation of the parallel triple-jet, Nuclear Engineering and Design, 249 (2012) 82-89.
- [9] N. Kimura, M. Nishimura, H. Kamide, Study on Convective Mixing for Thermal Striping Phenomena, Japan Society of Mechanical Engineers International Journal, 45(3) (2002) 592-599.
- [10] M. Nishimura, A. Tokuhiro, N. Kimura, H. Kamide, Numerical study on mixing of oscillating quasi-planar jets with low Reynolds number turbulent stress and heat flux equation models, Nuclear Engineering and Design, 202 (2000) 77-95.

- [11] N. Kimura, H. Miyakoshi, H. Kamide, Experimental investigation on transfer characteristics of temperature fluctuation from liquid sodium to wall in parallel triple-jet, *International Journal of Heat and Mass Transfer*, 50(9-10) (2007) 2024-2036.
- [12] I.S. Jones, M.W.J. Lewis, An Impulse Response Model for the Prediction of Thermal Striping Damage, *Engineering Fracture Mechanics*, 55(5) (1996) 795-812.
- [13] N. Kasahara, H. Takasho, A. Yacumpai, Structural response function approach for evaluation of thermal striping phenomena, *Nuclear Engineering and Design*, 212 (2002) 281-292.
- [14] R.E. Spall, E.A. Anderson, J. Allen, Momentum Flux in Plane, Parallel Jets, *Journal of Fluids Engineering*, 126(4) (2004) 665.
- [15] D. Tenchine, S. Vandroux, V. Barthel, O. Cioni, Experimental and numerical studies on mixing jets for sodium cooled fast reactors, *Nuclear Engineering and Design*, 263 (2013) 263-272.
- [16] S.-K. Choi, S.-O. Kim, Evaluation of Turbulence Models for Thermal Striping in a Triple Jet, *Journal of Pressure Vessel Technology*, 129 (2007) 583-592.
- [17] S.B. Pope, An Explanation of the Turbulent Round-Jet/Plane-Jet Anomaly, *American Institute of Aeronautics and Astronautics*, 16(3) (1978) 279-281.
- [18] H. Schlichting, *Boundary-Layer Theory*, 7 ed., McGraw-Hill Book Company, 1979.
- [19] J. Boulanger, L. Vervisch, J. Reveillon, S. Ghosal, Effects of heat release in laminar diffusion flames lifted on round jets, *Combustion and Flame*, 134(4) (2003) 355-368.
- [20] S.D. Hwang, H.H. Cho, Effects of Acoustic Excitation Positions on Heat Transfer and Flow in Axisymmetric Impinging Jet: Main Jet Excitation and Shear Layer Excitation, *International Journal of Heat and Fluid Flow*, 24(2) (2003) 199-209.
- [21] A. Pavlova, M. Amitay, Electronic Cooling Using Synthetic Jet Impingement, *Journal of Heat Transfer*, 128(9) (2006) 897.
- [22] N. Amini, Y.A. Hassan, Measurements of jet flows impinging into a channel containing a rod bundle using dynamic PIV, *International Journal of Heat and Mass Transfer*, 52(23-24) (2009) 5479-5495.
- [23] K.G. Condie, G.E. McCreery, H.M. McIlroy, D.M. McEligot, Development of an Experiment for Measuring Flow Phenomena Occuring in a Lower Plenum for VHTR CFD Assessment, in: D.o.E.O.o.N. Energy (Ed.), Idaho National Laboratory, Idaho Falls, Idaho 83415, 2005.
- [24] H.M. McIlroy, D.M. McEligot, R.R. Schultz, D. Christensen, R.J. Pink, R.C. Johnson, PIV Experiments to Measure Flow Phenomena in a Scaled Model of a VHTR Lower Plenum, in: D.o.E.O.o.N. Energy (Ed.), Idaho National Laboratory, Idaho Falls, ID 83415, 2006.

- [25] H. Haque, W. Feltes, G. Brinkmann, Thermal response of a modular high temperature reactor during passive cooldown under pressurized and depressurized conditions, *Nuclear Engineering and Design*, 236(5-6) (2006) 475-484.
- [26] K.L. McVay, J.-H. Park, S. Lee, Y.A. Hassan, N.K. Anand, Preliminary tests of particle image velocimetry for the upper plenum of a scaled model of a very high temperature gas cooled reactor, *Progress in Nuclear Energy*, 83 (2015) 305-317.
- [27] NASA jet Propulsion Laboratory Web Site in, 1997, pp. <http://masterweb.jpl.nasa.gov/reference/images/paints/Best%204%20paints%20MWIR.gif>.
- [28] D.T. Landfried, Experimental and Computational Studies of Thermal Mixing in Next Generation Nuclear Reactors, Doctorate of Philosophy, University of Pittsburgh, Pittsburgh, PA, 2015.
- [29] G.E. McCreery, K.G. Condie, Experimental Modeling of VHTR Plenum Flows During Normal Operation and Pressurized Conduction Cooldown, in: D.o.E.O.o.N. Energy (Ed.), Idaho National Laboratory, Idaho Falls, Idaho 83415, 2006.
- [30] S. Moriya, I. Ohshima, Hydraulic Similarity in the Temperature Fluctuation Phenomena of Non-Isothermal Coaxial Jets, *Nuclear Engineering and Design*, 120 (1990) 385-393.
- [31] R.S. Figliola, D.E. Beasley, *Theory and Design for Mechanical Measurements*, John Wiley & Sons, Inc., 2011.